Reduced Recombination Losses in Evaporated Perovskite Solar Cells by Postfabrication Treatment

David Kiermasch, Mathias Fischer, Lidón Gil-Escrig, Andreas Baumann, Henk J. Bolink, Vladimir Dyakonov, and Kristofer Tvingstedt*

The photovoltaic perovskite research community has now developed a large set of tools and techniques to improve the power conversion efficiency (PCE). One such arcane trick is to allow the finished devices to dwell in time, and the PCE often improves. Herein, a mild postannealing procedure is implemented on coevaporated perovskite solar cells confirming a substantial PCE improvement, mainly attributed to an increased open-circuit voltage (V_{OC}). From a V_{OC} of around 1.11 V directly after preparation, the voltage improves to more than 1.18 V by temporal and thermal annealing. To clarify the origin of this annealing effect, an in-depth device experimental and simulation characterization is conducted. A simultaneous reduction of the dark saturation current, the ideality factor (n_{id}), and the leakage current is revealed, signifying a substantial impact of the postannealing procedure on recombination losses. To investigate the carrier dynamics in more detail, a set of transient optoelectrical methods is first evaluated, ascertaining that the bulk carrier lifetime is increased with device annealing. Second, a drift-diffusion simulation is used, confirming that the beneficial effect of the annealing has its origin in effective bulk trap passivation that accordingly leads to a reduction of Shockley–Read–Hall recombination rates.

1. Introduction

Organic–inorganic hybrid perovskite solar cells have become a promising candidate for next-generation photovoltaic technology combining low fabrication costs and high power conversion efficiency (PCE) of more than 25%.[1] Now, PCEs, however, appear to have reached a saturation after an impressive initial development since the first use of methylammonium lead iodide (MAPbI₃) as a photoactive absorber in 2009.[2] Further increase in photovoltaic performance now requires a better understanding of the elementary physical processes governing the energy conversion, such as charge carrier generation, transport, and recombination dynamics. In case of the most common perovskite compositions such as MAPbI₃, characterized by a bandgap in the range of 1.6 eV, the maximum value of the short-circuit current (j_{SC}) corresponds to $\approx$25–26 mA cm^{-2}.[3] Several studies have already demonstrated currents close to 24 mA cm^{-2} in case of MAPbI₃[4] and even higher values[5] for lower bandgap perovskites comprising different organic molecules and halides, indicating that there is not much room for further j_{SC} improvements. Thus, to approach the PCE limit for a 1.6 eV bandgap material of 30.5%[3] according to Shockley–Queisser,[6] the other two photovoltaic parameters have to be addressed, namely, the fill factor (FF) and the open-circuit voltage.

The FF is to different extents limited by parasitic resistive losses such as shunt and series resistance (R_{shunt} and R_{series}) depending on the intensity that the solar cell is illuminated with. While leakage currents (due to a low R_{shunt}) are usually only limiting at very low illumination intensities,[7] losses due to R_{series} are almost always limiting at solar illumination intensities.[8] Minimizing Ohmic losses can be pursued by using transport materials with higher conductivity by, e.g., optimizing the established layer thickness and/or the doping level. The FF, however, also depends on the value of the n_{id}, which, in turn, is governed by the charge carrier recombination processes in the diode. In 1981, Green clarified that the FF of a solar cell can be simply described with knowledge of n_{id} and V_{OC} (and slightly more complex when both parasitic R_{shunt} and R_{series} are accounted for).[9] Higher FFs are obtained by pursuing an increased V_{OC} and a reduced n_{id}. It is, however, important to bear in mind[10] that a reduced ideality factor alone is not a sufficient aim to strive after, but only when it is accompanied with a reduced dark saturation current (j_0). Some recombination routes, such as surface recombination, can, e.g., progress faster but still operate through a low ideality factor. Accordingly, this will

D. Kiermasch, M. Fischer, V. Dyakonov, K. Tvingstedt
Experimental Physics VI
Julius-Maximilian University of Würzburg
97074 Würzburg, Germany
E-mail: ktvingstedt@physik.uni.wuerzburg.de

L. Gil-Escrig, H. J. Bolink
Instituto de Ciencia Molecular
Universidad de Valencia
46980 Paterna, Spain

A. Baumann
Bavarian Center for Applied Energy Research - Division Energy Efficiency
97074 Würzburg, Germany

The ORCID identification number(s) for the author(s) of this article can be found under https://doi.org/10.1002/solr.202100400.

be a low voltage cell, whose bad performance essentially has its origin in its large dark saturation current. If both j_0 and n_{id} can simultaneously be reduced, the V_{OC}, FF, and thus PCE per definition increase. In the pursued radiative limit of MAPbI$_3$, which corresponds to a V_{OC} of 1.33 V[11,12] the FF can exceed 90% at 1 sun illumination.[3,13] Considering the current state of the art perovskite photovoltaic devices, a further reduction of recombination losses is thus required for FF and V_{OC} and thus PCE improvements. For many perovskite devices, overall caution regarding accurate and true FF assignments is, however, always needed. With large numbers of mobile ions present in combination with fast surface recombination rates, the measured FF becomes heavily skewed by both the measurement speed and direction. The same goes with the employment of too small photomasks during characterization.[8]

The rate at which charge carriers recombine is usually described by the currently identified and understood different types of bulk loss mechanisms, that is, band-to-band radiative, Shockley–Read–Hall (SRH) and Auger recombination. In addition to bulk recombination losses, a prominent source of recombination can also often be found at the interface toward the surface or the electrodes present in devices. While it is always beneficial to minimize the defect-related nonradiative SRH and surface recombination losses, the higher order recombination mechanisms, band-to-band radiative and Auger recombination, are intrinsic material-dependent properties that cannot be avoided. To address losses due to suspected bulk recombination, the composition of the perovskite absorber has already been widely modified. Incorporation of cesium and rubidium into the crystal lattice pushed V_{OC} to 1.24 V for a 1.63 eV bandgap quadruple cation perovskite leading to a remarkable radiative efficiency of 3.8% due to a proposed reduction of trap states.[14–16] Along these initial reports, potassium iodide was also implemented as a bulk improving additive,[17] and similar additives are continuously being evaluated. The employment of these different components thus all aims to modify the bulk of the perovskite. However, a second route to reduce parasitic losses is to minimize surface recombination by passivating the interfaces between the perovskite and the adjacent charge transport layers. Long PL lifetimes over 8 μs under solar relevant carrier densities have, for example, been demonstrated on polycrystalline MAPbI$_3$ layers, if the surfaces were treated with passivating additives after preparation.[18] Successful surface passivation also recently assisted to approach the radiative limit with an internal quasi-Fermi level splitting of 1.28 eV.[19] Replacing PEDOT:PSS with p-TPD was also shown to reduce interface losses and increase the device voltage substantially.[7] Furthermore, a high open-circuit voltage of 1.21 V was realized by stacking a guanidinium bromide interface layer on top of a mixed-cation perovskite (featuring a bandgap of 1.62 eV).[20] The highest reported V_{OC} for MAPbI$_3$ so far is 1.26 V as recently reported by Liu et al.[21] This still exceptional photovoltage was achieved by a light-induced activation process; however, whose origin was not fully clarified. So far, these results demonstrate that new perovskite compositions, improved deposition methods, and interface engineering[22] are all indispensable means to push the PV efficiency closer to the sought-after radiative limit. The different remaining nonradiative recombination losses thus still stand as the main present and limiting factors in state-of-the-art perovskite solar cells, and whether bulk or surface recombination truly dominates is currently contested.[23]

Most of the aforementioned studies were based on solution-processed devices where the solute is annealed to around 100 °C to ensure material film crystallization. What is also frequently observed, yet not always reported with scrutiny, is the fact that an additional dwelling time of solution-manufactured devices appears to further improve the efficiency considerably. The origin of such storage-induced improvement is not fully examined, though the term "spontaneous healing" is sometimes perceived. Sodium ingress from the glass was initially suggested[24] to passivate defects by Bi et al., leading to an improvement mostly in j_{SC}. Crystal coalescence was also shown[25] to occur in time and was associated with an improved PCE, again mostly through a j_{SC} increase.[26] Similar observations exist, demonstrating instead that the V_{OC} of perovskite solar cells can increase during aging in the dark as well as by heating.[27,28] These improvements could be caused by the passivation of (bulk and surface) defects from small amounts of excess PbI$_2$ that appears as the perovskite starts to decompose.[29] Moghadamzadeh et al. performed thermally stimulated current (TSC) measurements, confirming a trap density reduction after 12 days of waiting, and they accordingly excluded surface passivation.[30] Cho et al. very recently[31] observed mainly V_{OC} improvements (in line with Moghadamzadeh) upon 2 days of storage, but proposed that this originated from both increased transport layer conductance, reduced surface recombination as well a simultaneous bulk trap passivation. Whether primarily surface or bulk improvements are mostly responsible for the increased performance upon waiting and heating is thus not yet fully clear. In our current work, we aim to describe how such a temporal and thermal annealing procedure is able to reduce recombination losses also in coevaporated planar n–i–p and p–i–n perovskite solar cells. We use methylammonium lead iodide (MAPbI$_3$) which is prepared by cosubliming PbI$_2$ and MAI in a high vacuum chamber integrated into a nitrogen-filled glove box. Unlike the first work in which MAI and PbCl$_2$[32] were used, we have consistently used both iodide precursors for this and previous studies.[33,34] The substrate temperature during vacuum deposition remains below 40 °C and as such is not expected to have a large influence on the annealing.

In our measured dark current–voltage characteristics, we observe a considerable reduction of both the saturation current density, the ideality factor as well as the leakage current, showing that recombination losses under both weak and strong (sunlight) illumination intensities are substantially minimized. Transient optoelectrical analysis is then performed to study the altered recombination dynamics in more detail, demonstrating that bulk recombination lifetimes are indeed increased by the postfabrication annealing process. Finally, the solar cells are evaluated by means of drift-diffusion simulations, which allow us to scrutinize what type of recombination is primarily being reduced upon annealing. To demonstrate that the induced increase in V_{OC} is not a temporary effect, stability measurements over more than half a year are also performed.

2. Results

Our study is conducted on coevaporated planar MAPbI$_3$-based n–i–p and p–i–n solar cells. Thick active layers (820 nm) are selected because the efficiency is increased and the analysis of the transient measurements is simplified compared with thinner

devices due to the smaller capacitance, as shown in a previous study.[35] The solar cells were fully evaporated with the fullerene C_{60} (partially doped with *N1,N4*-bis(tri-*p*-tolylphosphoranylidene)-benzene-1,4-diamine) as the electron transport layer (ETL) and the arylamine derivative *N4,N4,N4″,N4″*-tetra([1,1′-biphenyl]-4-yl)-[1,1′:4′,1″-terphenyl]-4,4″-diamine (TaTm, partially doped with 2,2′-(perfluoronaphthalene-2,6-diylidene) dimalononitrile) as the hole transport layer.[34] A schematic representation of the two studied device structures and details on their preparation is provided in the Supporting Information. For detailed information on the sublimation growth process, we refer the reader to the following reference.[36] After initial characterization, the devices were stored in a N_2-filled glove box, and when characterized as outlined later, always kept in inert atmospheres. Oxygen and humidity can thus with certainty be excluded from having an influence in this study. Current–voltage (*J–V*) characteristics under AM1.5G solar irradiation of the n–i–p and p–i–n devices directly after preparation are shown in **Figure 1**a). Both types of solar cells initially demonstrate quite similar open-circuit voltages slightly exceeding 1100 mV. Differences in FF (72% for n–i–p and 70% for p–i–n) and j_{SC} (22.7 mA cm^{-2} for the n–i–p and 20.2 mA cm^{-2} for the p–i–n) lead to different PCEs ranging from ≈18% for the n–i–p device to −16% for the p–i–n configuration. The larger current of the n–i–p cell originates from less parasitic light absorption in the transport layers. While the illuminated n–i–p device showed minor but still detectable hysteresis, the p–i–n cell did not display any discernable differences between the initial forward and backward scan. The dark *J–V* of the p–i–n cell also showed no initial hysteresis, which then regrettably grew more pronounced in time. As the dark *J–V* of the n–i–p device showed no hysteresis at all during the entire time frame of our study, our main recombination results will be based on the interpretation of this device. Figure 1b shows the evolution of V_{OC} for both solar cells during the time after preparation and the conduction of a simple mild postannealing procedure after a few days. The mild thermal

annealing of the completed devices was performed inside a closed helium cryostat, where the temperature was slowly increased from 300 up to just 320 K, at which the solar cells were then kept for several hours, followed by cooling down to room temperature again. The temperature was not increased to further higher values as it is known that heating of MAPbI$_3$ devices over 363 K leads to irreversible degradation.[27,37] Already prior to the annealing, a steep rise in V_{OC} can be observed where the initial voltage of around 1110 mV increases to approximately 1140–1150 mV. Thermal annealing then improves the V_{OC} even further to more than 1180 mV, a value that was subsequently confirmed to be stable for more than half a year. The red arrows in Figure 1b indicate the day the postannealing was conducted. To disentangle the processes of time and heating, the V_{OC} development of an identical additional n–i–p device without the thermal annealing treatment was evaluated simultaneously. For this device, the voltage stabilizes at around ≈1150 mV after 100 days. We therefore conclude that the processes increasing the voltage from ≈1110 to ≈1150 mV are mostly time-induced as indicated by the gray area, while a further small improvement from ≈1150 to ≈1180 mV is actuated by the mild thermal annealing procedure (red area).

To gain more insight into the origin of the V_{OC} improvement, we start by assessing the recombination behavior of the two devices via their dark *J–V* curves. **Figure 2** shows the dark current–voltage scans of the two devices, performed within the period between 0 and 111 days. The mild heating step is indicated with a red arrow that separates the measurement before and after the heating. For clarity, only measurements from the forward scan direction between −0.2 and 1.5 V are shown here. The full set of forward and backward scans is provided in Figure S3, Supporting Information. The red-dashed lines are fitted curves corresponding to the generalized Shockley equation (Equation (1)), accounting not only for the underlying recombination mechanisms responsible for the observed V_{OC} changes, but also for resistive effects
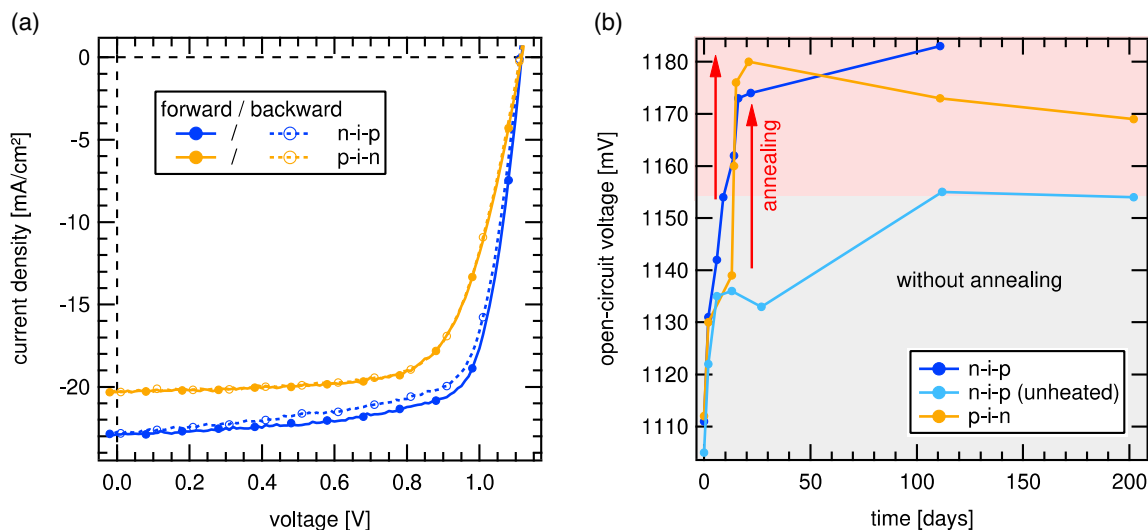
Figure 1. a) *J–V* characteristics of n–i–p and p–i–n solar cells after preparation, determined under 1 sun illumination. b) V_{OC} evolution during a time span of 202 days for both types of devices. The postannealing procedure (heating to 320 K for several hours and cooling down back to 300 K) is indicated by the red arrows. As reference, the V_{OC} development for an n–i–p device without heat treatment is shown, demonstrating that the voltage improvement is less than for the heated cells.
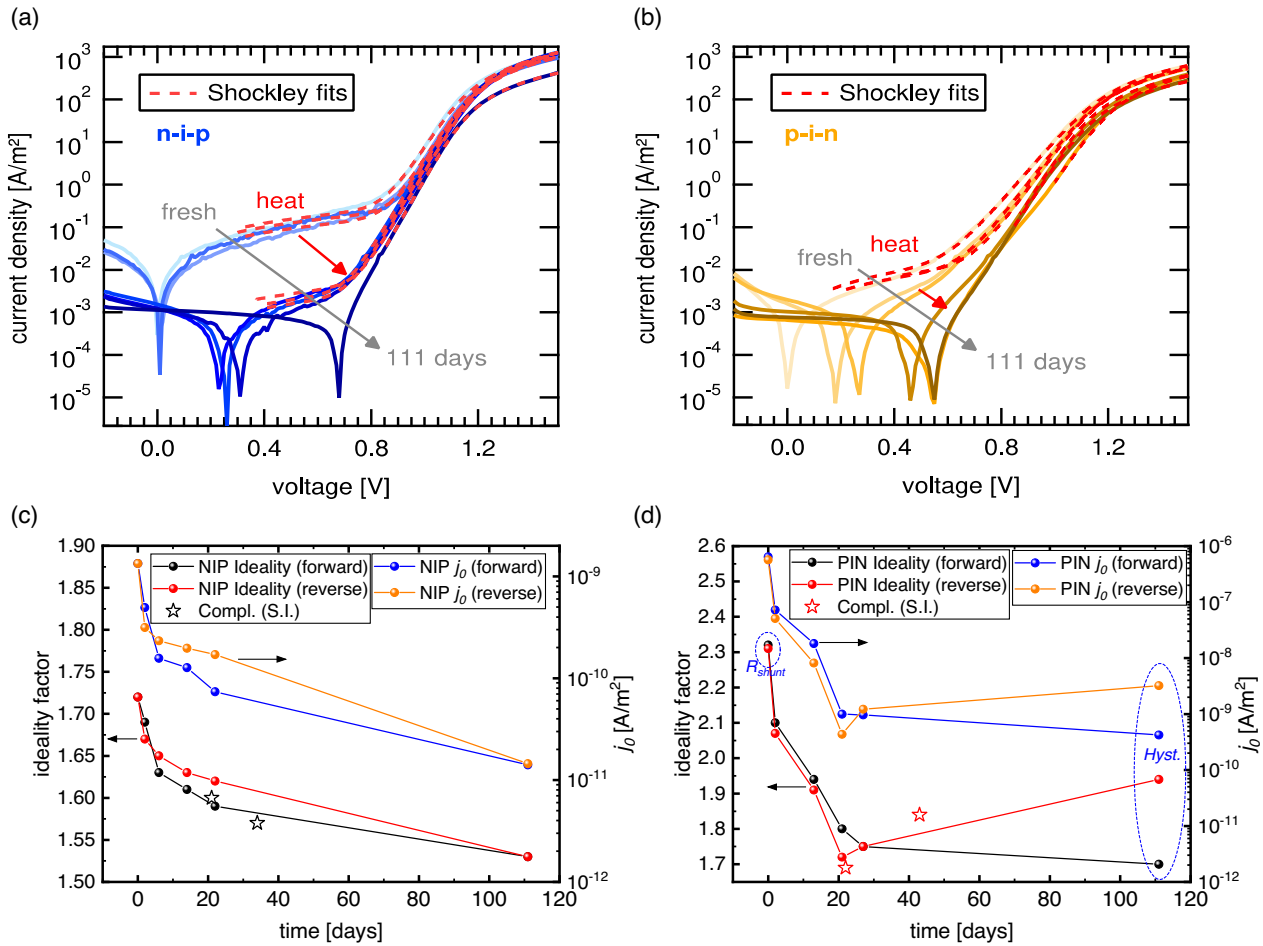
Figure 2. a,b) Dark *J–V* (forward scans) fitted with the generalized Shockley equation for the two cells as they develop in time and with heating. c,d) The corresponding Shockley diode recombination parameters for the two devices (from both forward and reverse scans). A continuous and linked reduction of the dark saturation current (j_0) and the ideality factor is confirmed and analyzed further in Figure 3. The ideality factor was additionally determined with complementary methods unaffected by series resistance, as outlined in Figure S5, Supporting Information and included as stars in (c) and (d).

$$j = j_0 \cdot \left(e^{\frac{q(V - jR_{series})}{n_{id}kT}} - 1 \right) + \frac{V - jR_{series}}{R_{shunt}} \qquad (1)$$

The influence of the shunt and series resistances and how they alter in time and due to heating is outlined in more detail in Figure S4, Supporting Information. Initial data about the altering recombination processes can now be retrieved by examining the exponential part of the dark *J–V* curves with focus on the dark saturation current j_0 and the ideality factor n_{id}. Details on the general relationships between ideality factor and the dominant recombination processes are provided in the literature.[10,35,38] The values of j_0 and n_{id} from the two studied devices are shown in Figure 2c,d and show a noticeable and apparently linked reduction within the studied time span. It is obvious that the changes in dark saturation current and ideality factor, due to time and annealing, are in line with the observed improvements in V_{OC}, confirming that the recombination dynamics are changing very beneficially in both devices upon the temporal and thermal annealing. For the n–i–p cell, n_{id} decreases from 1.73 to 1.53, while the p–i–n device exhibits reduction from 2.30 to 1.69.

We here note that although we try to account for the parasitic resistances in our determination of the ideality factor, we acknowledge that the earliest data are still partially elevated by the very low shunt resistance, which, however, disappeared after the heating step. Prior to the heating step, the shunt resistance does, furthermore, not appear to be fully ohmic for the p–i–n cell, likely augmenting the perceived hefty value of 2.3.

In the case of a solar cell operating in the pursued radiative limit, where all recombination originates from pure radiative band-to-band transitions, the ideality factor equals unity and the dark saturation current $j_0 = j_{0,Rad}$, embodying a parameter that can be determined from reciprocity relations as conducted previously.[11] The radiative recombination current can also be directly measured in absolute terms, and stands as the ultimate recombination reference of a fully optimized solar cell. For the n–i–p device, we have in **Figure 3** thus replotted the data together with the measured radiative recombination reference curve, as the sought-after comparison toward which the dark *J–V* curve should strive. By comparing the dark *J–V* curves to the radiative recombination curve, we can clearly see how the annealing and
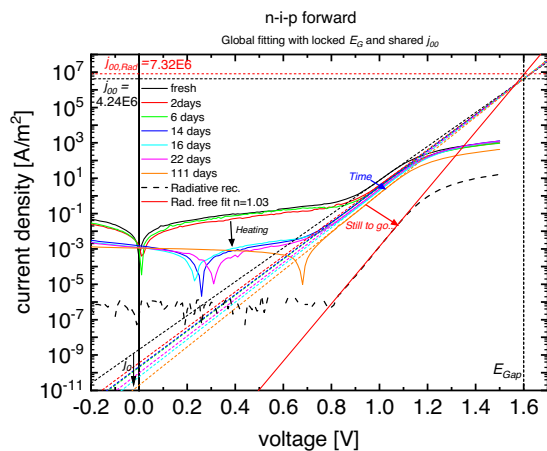
Figure 3. The dark J–V curves of the n–i–p cell now together with the external radiative recombination current (black thick dashed), as measured via absolute electroluminescence flux. The dark J–V curves are fitted (dashed thin lines) with a global data fitting routine, according to Equation (2), where only the ideality factor is an allowed free fit parameter for each curve. The bandgap was locked at 1.60 eV and the j_{00} value set as joint fit parameter with an obtained value of 4.24×10^6 Am^{-2} with a standard deviation of only 2%. This high confidence level ascertains that the falling dark saturation current (j_0) is thus a mere consequence of the decreasing ideality factor. We highlight that j_{00} and $j_{00,\text{Rad}}$ (obtained by extrapolating the radiative curve) are very close to each other.

time reduce the nonradiative recombination such that we are approaching, but by no means reaching, the radiative limit. The ratio of the radiative recombination to the total recombination represents the radiative efficiency,[11] in the case of injection; electroluminescence efficiency EQE$_{\text{EL}}$. The determined EQE$_{\text{EL}}$ for both devices after postannealing is shown in Figure S5b and S6, Supporting Information. At an injection current which corresponds to j_{SC} at 1 sun (and therefore a charge carrier density under realistic operating conditions), the solar cells show a high radiative efficiency of around 1%, which increases up to 1.8% for a higher driving voltage of 1.5 V. These numbers are comparable with the highest efficiencies reported so far of 1% for a quadruple cation perovskite (containing Rb, Cs, MA, FA, I, and Br),[14] 7% for FA$_{0.92}$MA$_{0.08}$PbI$_3$[39] and 8% for MAPbI$_3$.[21]

The most significant feature of Figure 3, associated with the simultaneous and linked reduction of j_0 and n_{id}, is, however, the identification of their common origin. By extrapolating the exponential parts of the dark J–V curves and the radiative recombination current curve toward higher voltages and currents, a common intersecting point can be identified. Mathematically, this corresponds to factorizing the constituents[40] of the dark saturation current j_0, allowing us to rewrite the dark Shockley diode equation

$$j(V) = j_0 \cdot e^{\frac{qV}{n_{\text{id}}kT}} = j_{00} \cdot e^{\frac{qV - E_A}{n_{\text{id}}kT}} \qquad (2)$$

in terms of the activation energy for recombination E_A as well as a prefactor j_{00}. At a voltage value corresponding to E_A, for this material and device ≈ 1.60 eV, we can forthright and perhaps unsurprisingly conclude that the relevant activation energy indeed equals the bandgap energy, $E_A = E_{\text{Gap}}$. Accordingly, this

parameter is not changing during the temporal and thermal annealing. Acknowledging this fact, we proceed by conducting a global fitting of all measured dark J–V curves with Equation (2), wherein we lock the value of E_A to $E_G = 1.60$ eV, share the j_{00} prefactor, and allow only the slope, i.e., the ideality factor to alter independently (the data presented in Figure 2c). The intersecting point thus allows us to estimate the single joint value on the ordinate axis, namely, the j_{00} value. j_{00} corresponds to the fictional recombination current that would flow in a device, should the maximum allowed density of states (DOS) be filled.[40] $j_{00,\text{Rad}}$ likewise corresponds to the radiative current that would flow in the device, should the DOS be filled. Unlike j_{00}, the value of $j_{00,\text{Rad}}$ can be directly estimated from detailed balance theory. Its value must be related to the product of the DOS and the known radiative rate constant according to

$$j_{00,\text{Rad}} = q \cdot d \cdot k_{\text{Rad}} \cdot N_C N_V \qquad (3)$$

where d is the film thickness and q the elementary charge (converting volume rates into current densities), k_{Rad} the radiative rate constant, and N_V and N_C are the valence and conduction bands DOS, respectively. From Figure 3 we can in fact settle that for these studied perovskite devices, j_{00} and $j_{00,\text{Rad}}$ entails essentially similar values. We note that this is in strong contrast to organic solar cells, where a difference of several magnitudes between j_{00} and $j_{00,\text{Rad}}$ was observed,[40] demonstrating that organic and (these) perovskite photovoltaic devices are limited by very different nonradiative recombination mechanisms. The prevailing difference in radiative and nonradiative recombination currents seen in organic solar cell even at carrier densities approaching a filled DOS supports that the nonradiative recombination in those materials indeed has an intrinsic[41] origin. This is apparently not the case for the perovskite devices studied herein, as j_{00} and $j_{00,\text{Rad}}$ are almost identical. The observation of the increased V_{OC} obviously has its sole origin in the increased slope (decreased n_{id}) of the dark J–V curve, causing an ensuing exponentially reduced value of the dark saturation current j_0. Such simultaneous decrease in j_0 and n_{id}, without any observable alteration of neither activation energy nor DOS, must thus be correlated with extrinsic properties, usually in the form of deep defects. The observed reduced recombination rate upon time and heating therefore most likely has its origin in a reduced concentration of bulk defects, or a reduction of their corresponding capture cross section. In any case, this is the first sign that nonradiative SRH recombination is efficiently decreased by the introduced postannealing procedure. (A similar analysis would partly also apply to the p–i–n cell data, yet due to the increasing amount of hysteresis, and more fluctuating shapes of the dark J–V curves, it would be less definite as for the here presented n–i–p cell.)

To extend the analysis of the reduced charge carrier recombination processes, we further evaluated the devices with transient optoelectrical techniques, namely, transient photovoltage (TPV) and charge extraction (CE) to determine the charge carrier lifetime at each corresponding charge carrier density. In CE, the photovoltaic device is held at open-circuit voltage conditions under constant illumination. A fast (nanosecond) switch is then used to turn off the light and rapidly switch the device to short-circuit conditions. The resulting current pulse from the cell is

then integrated and normalized to the volume of the film to obtain the effective charge carrier density n at the preceding V_{OC} condition. Repeating the experiment for a large range of illumination intensities allows us to plot the calculated carrier densities over the corresponding voltages, as shown in **Figure 4**. We note that under higher illumination conditions, the solar cells are slightly heated up by the used LED, even though the measurements were performed in a closed cycle helium cryostat. To account for this extra heating we calculated and used instead the isothermal open-circuit voltages on the x-axis according to the method outlined before.[35,42]

Filled circles summarize the CE measurements performed under illumination intensities in the range of 10^{-5} up to 3 suns, and the dashed lines correspond to measurements in the dark. The latter are performed to determine the amount of charge carriers associated with the geometric capacitance of the electrodes. Here, the charge carriers stored on the electrodes are extracted by applying a small negative bias without illumination prior to switching to short-circuit conditions. The reverse bias condition prevents diode carrier injection, but is assumed to generate an identical geometric capacitance as under (the illuminated) forward bias condition. Under illumination, both bulk carriers and capacitive carriers are measured. We can see that both devices show a transition from a shallow to a steeper slope at around 1.05 V. At lower voltages, only minor differences between the illuminated and dark measurements can be observed, while at higher voltages the light induces a substantial increase in charge carrier density. In line with previous studies,[35,43] we conclude that mostly capacitive charge carriers rule these measurements at lower voltages. For the p–i–n solar cell, the similarity between the geometric capacitance and the charge carrier density obtained under illumination ($V_{OC} \leq 1.05$ V) is pointing toward a pure geometric capacitance origin. In contrast, a small but discernable voltage-dependent offset is identified in the n–i–p cell at voltages below 1.05 V, which results from an additional type of capacitive

contribution. These charges probably have their origin in some form of depletion-layer capacitance in the film, as already proposed for perovskite solar cells under certain conditions.[44] It is therefore important to note that even though the same transport layers have been used and the perovskite layer was prepared in the same evaporation run, the two devices show quite different capacitive characteristics. The postannealing procedure does, however, not at all influence the voltage dependence of the capacitive charge carriers (low voltages). This is contrary to the high voltage regime, where charge carriers from the bulk dominate the dynamics.[35,43] Here, a pronounced difference in the extracted amount of charge carriers can be confirmed, clearly pointing toward significantly modified recombination kinetics by the postannealing procedure.

To best probe these altered kinetics, the charge carrier lifetimes must be evaluated at each measured carrier density, and we thus use TPV to pursue this goal. Then, the solar cells are illuminated with the same illumination intensity that was used for CE. After reaching a steady-state open-circuit voltage (usually within a millisecond timescale in these devices) from the LED light, additional charge carriers are now generated by a 80 ps short laser pulse. The decay of this additionally (small perturbation) created photovoltage ΔV_{OC} is subsequently fitted with an exponential decay to determine the small perturbation carrier lifetime. The technique of TPV has been widely used to study thin-film devices such as organic or perovskite photovoltaics, yet there are several reports about the limitations that this measurement method entails. It has, e.g., been suggested that spatially inhomogenous charge carrier distributions[45] (especially at low illumination intensities) induced by thin layers and/or doping can lead to an overestimation of carrier lifetimes and to an unrealistic high recombination order.[46] Such capacitive limitations due to electrodes or the depletion layer of a junction can dominate the measured voltage decay lifetimes, making it difficult to interpret the charge carrier lifetime correctly.[43,47]
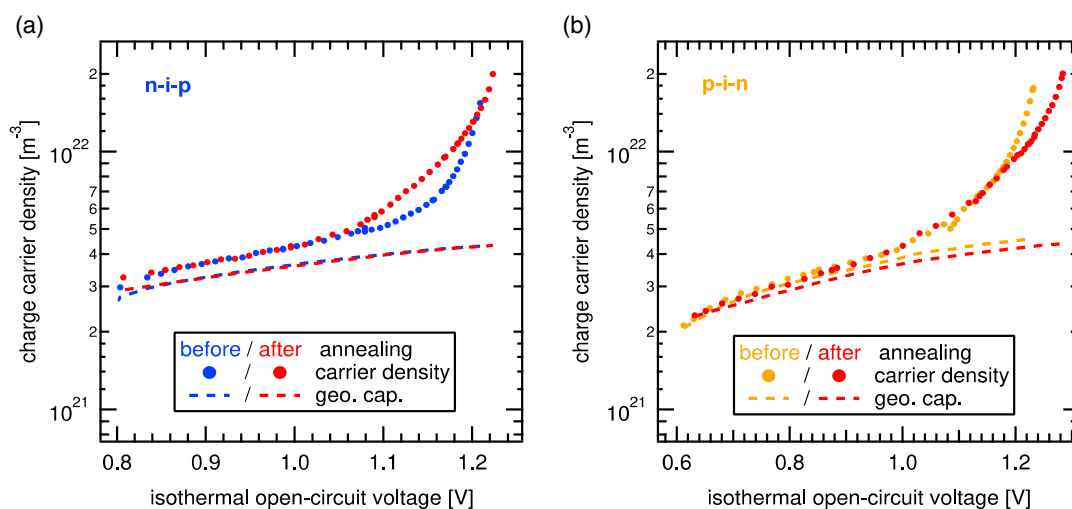
Figure 4. Charge carrier density from CE plotted versus the open-circuit voltage for the a) n–i–p and b) p–i–n devices before (blue/orange filled circles) and after (red filled circles) annealing. In both types of devices, a clear transition from a shallow slope at low voltages ($V_{OC} \leq 1.05$ V) to a steeper slope at higher light intensities can be observed. Dashed lines represent extracted charge carrier density from geometric capacitance measured by CE in the dark. While the low-voltage part of the extracted carrier densities for the p–i–n device almost coincides with the geometric capacitance values, a notable voltage-dependent offset is observed for the n–i–p cell.

Trapping and release of charge carriers in shallow trap distributions can, however, also prolong the lifetime in a similar fashion, as proposed by Du et al.[48] To reduce any capacitance complications, the active layer thickness of the herein studied devices is manufactured with a thickness exceeding 800 nm, significantly higher than most devices, such that the assumption of a homogenously distributed excess carrier concentration (important to also calculate the previously discussed charge carrier densities correctly) gets more justified. To compare the change in carrier dynamics induced by the postannealing, we analyze how the lifetime scales with carrier density (rather than voltage) as shown in **Figure 5** for both devices, together with the limit from the geometric capacitance.

In both kinds of solar cells, the measured lifetimes are close to the capacitive limit for densities below 4×10^{21} m^{-3} (capacitive regime in gray identified with the dashed lines in Figure 4). Here, the postannealing process does not influence the capacitive discharging "lifetimes," whereas the true bulk carrier lifetimes, probed above 4×10^{21} m^{-3}, are noticeably increased. In the capacitive regime, the "lifetimes" scales very steeply with carrier density, while the slope gets much shallower for concentrations above 4×10^{21} m^{-3}. As already discussed in previous works, this slope only represents a useful indicator of the dominant carrier recombination mechanism if bulk charge carriers are exclusively measured.[35,43] Comparing the two curves in Figure 5a (the n–i–p cell) in this relevant regime (above 4×10^{21} m^{-3}), the effect of the postannealing treatment can be clearly identified, as not only overall longer lifetimes are measured, but also a steeper slope can be identified.

The increased slope, confirming a transition from an almost carrier density independent lifetime, to a density dependent one, thus allows us to conclude that the postannealing process indeed increases the dominant recombination order, clearly at least in the n–i–p device. This is expected, if fast first-order SRH

recombination centers have been passivated and are further in line with the observed reduction of n_{id} in Figure 2. The transient optoelectrical analysis directly proves that the reason for the increase in V_{OC} (see Figure 1b) in both devices has its origin in an improved carrier lifetime and an associated reduced recombination rate. Our measured lifetimes are further in good agreement with calculations from Pazos-Outoón et al., confirming that a SRH lifetime of around 800 ns should yield an open-circuit voltage of around 1.19 V with MAPbI$_3$ as an active layer material under 1 sun illumination conditions.[49] The measured lifetimes are among the highest carrier lifetimes reported so far for pure iodide-based perovskite solar cells, raising the hope that further improvements should be within reach as SRH lifetimes exceeding 10 μs will increase V_{OC} substantially closer toward the radiative limit.[13]

As outlined earlier, perovskites are in contemporary literature described as being limited by both SRH trap-assisted recombination and surface recombination. Here, we have experimentally already shown that the simultaneous reduction of both the dark saturation current and the ideality factor strongly indicates primarily a reduction of SHR bulk recombination, demonstrating that this was the dominant loss, at least prior to annealing. If the cells would initially have been mostly limited by surface recombination, and the annealing reduced this limitation, we would indeed expect an increased lifetime and a reduction of j_0, but not expect to see an increase in the recombination order and a reduction of the ideality factor. Yet, as surface recombination is recurrently suggested as a dominant limiting factor in many high-performance solar cells, we would thus now like to dig a bit deeper into these aspects. To elucidate the altered recombination dynamics a bit further, we now aim to simulate the impact of the annealing on the dark diode characteristics with a drift-diffusion model. We start by studying the J–V characteristics where the overall recombination is comparatively small,
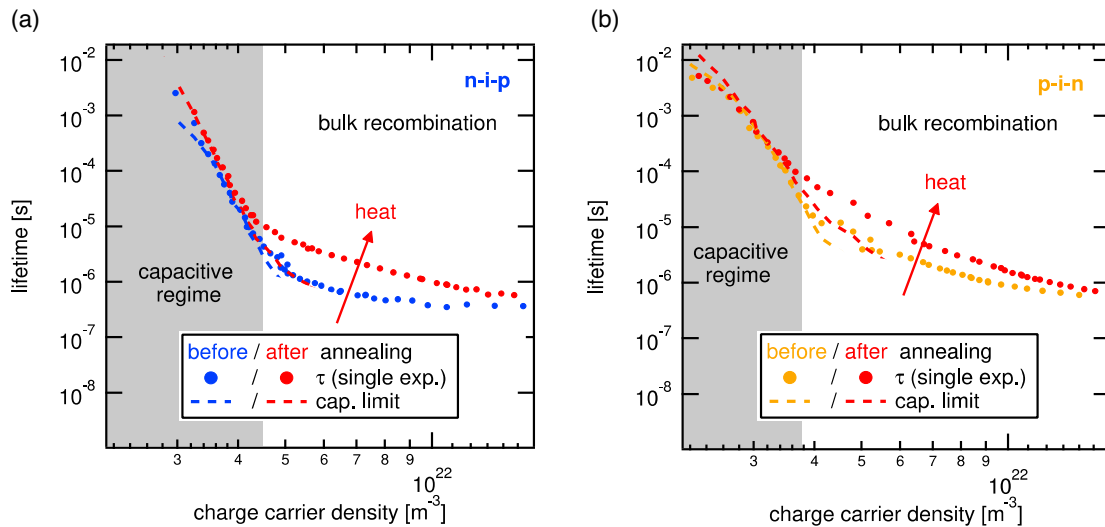
Figure 5. Charge carrier lifetimes as determined from single exponential fits plotted over the charge carrier density for the a) n–i–p and b) p–i–n device. Dashed lines correspond to the capacitive discharging time, which was calculated as previously reported.[43] At lower charge carrier densities ($\leq 4 \times 10^{21}$ m^{-3}), the measured data originate from the recombination of spatially separated capacitive charge carriers, while relevant bulk carrier dynamics can be detected at higher densities. Charge carriers from the bulk demonstrate that postannealing leads to a higher carrier lifetime at the same density, which accordingly results in an improved open-circuit voltage under operating conditions (cf., Figure 1b).

and then increase the rate of a single suspected culprit at a time, such that the direct influence of individual recombination mechanisms can be monitored independently. Therefore, we have chosen the experimentally measured J–V curve of the 22-day aged n–i–p device as a starting point, and fitted it with a newly developed drift-diffusion model[50] that accounts for radiative, SRH bulk, and surface recombination with the parameters shown in Table S1, Supporting Information. Then, from this best performing curve, we choose to increase the recombination rate associated with either bulk SRH or surface recombination, which thus allows us to, independently, visualize the different impacts of these two loss processes. (We note that we in the simulations always have to assume a very low level of incident background light responsible for generating the nonzero V_{OC} observable in these "dark" measurements.) The results are shown in **Figure 6**, where increased surface recombination velocity ν and reduced bulk SRH lifetime τ show fundamentally different impact on the dark J–V curve.

As shown in Figure 6a, increased surface recombination leads to divergent slopes, rendering increasing values of j_{00}, and is therefore certainly not in agreement with the experimental findings shown in Figure 3. However, if only the bulk SHR lifetime is changed (as shown in Figure 6b), the J–V curves still point to a common j_{00} when extrapolated to a voltage corresponding to the bandgap energy, in very good agreement to what was observed in the real devices during aging/heating.

Finally, the structural origin of the suggested reduced SRH rates induced by the thermal postannealing process will be discussed in the context of the current literature. A plausible explanation could be found in the induced changes by the tetragonal–cubic phase transition, which occurs at approximately 310–338 K and therefore in the range of the postannealing temperature of 320 K.[51–53] However, it has been indicated for MAPbI$_3$ that no abrupt optical changes seem to take place across this phase transition, but only that the ion activation energy decreases (at approximately 318 K) which is probably not relevant for the herein observed phenomena.[54] This is in line with another report,[53] where the solar cell performance has been

studied in the temperature range of 298–343 K. It was found that the phase transition did not lead to any discontinuity in device performance, indicating that optoelectronic properties are largely insensitive to this particular phase transition. Interestingly, some devices in mentioned study also showed an improvement in V_{OC} after heating and cooling back, which the authors, however, did not pay attention to. These prior observations lead us to the conclusion that the phase transition is probably not the origin of the performance improvements.

Recently, Tsai et al. showed how light-induced lattice expansion can help to improve the PCE and in particular the V_{OC} of MAPbI$_3$ and mixed perovskites.[55] It was suggested that a decrease in the energetic barrier near the perovskite interfaces and the reduction of nonradiative recombination both in the bulk and at the interfaces are the reason for the observed device improvements. This is in line with other reports,[56] where the impact of crystal strain on recombination dynamics has been studied, demonstrating that strain-free films and devices are associated with reduced defect concentrations. This coincides with the work by Nishimura et al., where the effect of lattice strain on Sn-based perovskite solar cells was investigated by substituting different cations.[57] They found a strong correlation between strain and the device efficiency and concluded that strain-free devices provide the highest PCE (and V_{OC}). Local strain inhomogeneities could very well be linked with energetic potential wells or active recombination centers that forms already during device preparation. This is supported by that the volumetric expansion coefficient α_V for MAPbI$_3$ is significantly higher compared with other thin-film solar cell materials such as CIGS or CdTe as reported by Jacobsson et al.[51] and a higher expansion coefficient increases the probability of removing crystal strain if the temperature is increased. Recently, Lohmann and coworkers studied the effect of different substrate temperatures during coevaporation on the performance of vacuum deposited MAPbI$_3$ solar cells.[58] By varying the temperature from 271 to 296 K, a strong correlation with the PCE was found, demonstrating that a higher substrate temperature indeed improves the device, which supports the herein presented findings.
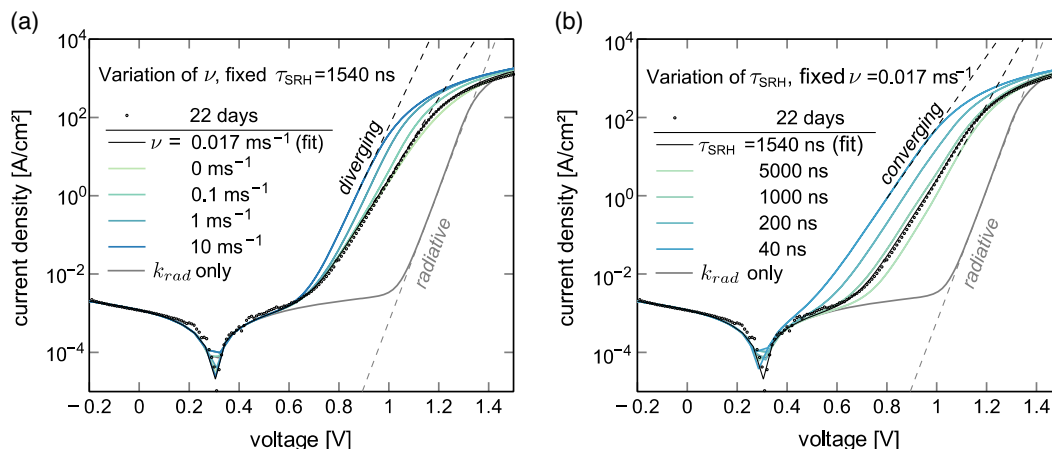
Figure 6. Dark J–V curves simulated with the parameters obtained by fitting the measured reverse dark J–V of the 22 days aged n–i–p device. In panel a) we increased the surface recombination velocity ν and kept the other fitted values constant. In panel b) we kept the surface recombination velocity constant and allowed instead only a reduction of bulk SRH lifetimes τ. Although both cases render faster total recombination, it is evident that the altering of SRH lifetimes in panel b) is in best agreement with the experimental result observed in Figure 3.

We therefore argue that the release of strain, upon heating the perovskite film, effectively seems to passivate bulk defects induced by perovskite lattice discontinuities, thus reducing the SRH recombination rates. Our work underlines that further research on perovskite PV does not exclusively have to focus on optimizing material combinations and preparation routes, but also on simple postprocessing methods such as illumination with light,[21,55] treatment of the perovskite surface with other solutions,[59] or postannealing in solvent atmosphere.[60]

3. Conclusion

We herein evaluate the effect of device temporal and thermal annealing of planar coevaporated n–i–p and p–i–n perovskite solar cells. We show that the open-circuit voltage can be improved from 1110 mV to more than 1180 mV by storing the devices in a nitrogen-filled glove box and annealing to 320 K and cooling back to 300 K again. Current–voltage characteristics in the dark revealed a considerable increase in the shunt resistance, proving that leakage currents were reduced by up two orders of magnitude. The J–V curves are primarily analyzed with respect to the dark saturation current and ideality factor, which show a linked and simultaneous reduction, pointing toward decreased SRH recombination losses. Stability measurements over more than half a year and MPP tracking confirmed that the increase in performance was also a permanent feature. Recombination dynamics is investigated in more detail by the transient optoelectrical techniques TPV and CE, allowing us to demonstrate that the charge carrier lifetime increases with postannealing, which is an indication of a reduced amount of traps or their capture cross section. To ascertain our assignment of reduced SRH recombination, we further model our devices with drift-diffusion simulations, and conclude that our experimental observations are indeed only compatible with such losses, as opposed to reduced surface recombination. Our conducted measurements and simulations show that nonradiative recombination certainly is being reduced in time. In addition, it would, however, also have been justified to fully monitor how the radiative recombination (or absorptance or EQE tails) developed during the time study, to further probe to what possible extent these properties could have altered. Reduction of radiative recombination would, however, have been expected to mostly shift the curves in Figure 3, and not to alter their slopes. This figure thus therefore points toward a mainly unaltered radiative recombination with its constant effective E_G and j_{00}, but direct EQE tail measurements would have better certified this. We therefore propose this as a motivated future study on the topic. A high radiative efficiency of more than 1% was nonetheless determined from electroluminescence measurements, showing that the set of improved devices is quite competitive with the most efficient multication perovskite PVs reported so far. Finally, possible structural reasons, such as a temperature-induced release of strain in the perovskite film, are suggested as a plausible origin for the observed phenomena. It is therefore proposed that future works on perovskite solar cells should consider postannealing steps after preparation or control the substrate temperature during manufacturing to reduce in operando recombination losses.

4. Experimental Section

Device preparations, measurement routines, and simulation conditions are specified in detail in the Supporting Information.

Supporting Information

Supporting Information is available from the Wiley Online Library or from the author.

Conflict of Interest

The authors declare no conflict of interest.

Author Contributions

L.G.E.: manufactured the devices in Valencia, which D.K. measured in Würzburg. M.F.: conducted the simulations. D.K., M.F., and K.T.: analyzed the data and wrote the article, to which all authors contributed with feedback and comments.

Data Availability Statement

The data that support the findings of this study are available from the corresponding author upon reasonable request.

[1] M. A. Green, E. D. Dunlop, J. Hohl-Ebinger, M. Yoshita, N. Kopidakis, X. Hao, *Prog. Photovoltaics Res. Appl.* **2020**, *28*, 629.

[2] A. Kojima, K. Teshima, Y. Shirai, T. Miyasaka, *J. Am. Chem. Soc.* **2009**, *131*, 6050.

[3] W. Tress, in *Organic-Inorganic Halide Perovskite Photovoltaics*, (Eds: N.-G. Park, M. Grätzel, T. Miyasaka), Springer International, Switzerland **2016**, p. 53.

[4] a) D. Y. Son, J.-W. Lee, Y. J. Choi, I.-H. Jang, S. Lee, P. J. Yoo, H. Shin, N. Ahn, M. Choi, D. Kim, N.-G. Park, *Nat. Energy* **2016**, *1*, 16081; b) S. S. Shin, E. J. Yeom, W. S. Yang, S. Hur, M. G. Kim, J. Im, J. Seo, J. H. Noh, S. I. Seok, *Science* **2017**, *356*, 167.

[5] W. S. Yang, J. H. Noh, N. J. Jeon, Y. C. Kim, S. Ryu, J. Seo, S. I. Seok, *Science* **2015**, *348*, 1234.

[6] W. Shockley, H. J. Queisser, *J. Appl. Phys.* **1961**, *32*, 510.

[7] K. Tvingstedt, L. Gil-Escrig, C. Momblona, P. Rieder, D. Kiermasch, M. Sessolo, A. Baumann, H. J. Bolink, V. Dyakonov, *ACS Energy Lett.* **2017**, *2*, 424.

[8] D. Kiermasch, L. Gil-Escrig, H. J. Bolink, K. Tvingstedt, *Joule* **2019**, *3*, 16.

[9] M. A. Green, *Solid-State Electron.* **1981**, *24*, 788.

[10] P. Caprioglio, C. M. Wolff, O. J. Sandberg, A. Armin, B. Rech, S. Albrecht, D. Neher, M. Stolterfoht, *Adv. Energy Mater.* **2020**, *10*, 2000502.

[11] K. Tvingstedt, O. Malinkiewicz, A. Baumann, C. Deibel, H. J. Snaith, V. Dyakonov, H. J. Bolink, *Sci. Rep.* **2014**, *4*, 6071.

[12] W. Tress, N. Marinova, O. Inganäs, M. K. Nazeeruddin, S. M. Zakeeruddin, M. Graetzel, *Adv. Energy Mater.* **2015**, *5*, 1400812.

[13] W. Tress, *Adv Energy Mater.* **2017**, *7*, 1602358.

[14] M. Saliba, T. Matsui, K. Domanski, J.-Y. Seo, A. Ummadisingu, S. M. Zakeeruddin, J.-P. Correa-Baena, W. R. Tress, A. Abate, A. Hagfeldt, M. Grätzel, *Science* **2016**, *354*, 206.

[15] Y. Hu, E. M. Hutter, P. Rieder, I. Grill, J. Hanisch, M. F. Aygüler, A. G. Hufnagel, M. Handloser, T. Bein, A. Hartschuh, K. Tvingstedt, V. Dyakonov, A. Baumann, T. J. Savenije, M. L. Petrus, P. Docampo, *Adv. Energy. Mater.* **2018**, *8*, 1703057.

[16] M. Saliba, T. Matsui, J.-Y. Seo, K. Domanski, J.-P. Correa-Baena, M. K. Nazeeruddin, S. M. Zakeeruddin, W. Tress, A. Abate, A. Hagfeldt, M. Grätzel, *Energy Environ. Sci.* **2016**, *9*, 1989.

[17] M. Abdi-Jalebi, Z. Andaji-Garmaroudi, S. Cacovich, C. Stavrakas, B. Philippe, J. M. Richter, M. Alsari, E. P. Booker, E. M. Hutter, A. J. Pearson, S. Lilliu, T. J. Savenije, H. Rensmo, G. Divitini, C. Ducati, R. H. Friend, S. D. Stranks, *Nature* **2018**, *555*, 497.

[18] D. W. deQuilettes, S. Koch, S. Burke, R. K. Paranji, A. J. Shropshire, M. E. Ziffer, D. S. Ginger, *ACS Energy Lett.* **2016**, *1*, 438.

[19] I. L. Braly, D. W. deQuilettes, L. M. Pazos-Outón, S. Burke, M. E. Ziffer, D. S. Ginger, H. W. Hillhouse, *Nat. Photonics* **2018**, *12*, 355.

[20] D. Luo, W. Yang, Z. Wang, A. Sadhanala, Q. Hu, R. Su, R. Shivanna, G. F. Trindade, J. F. Watts, Z. Xu, T. Liu, K. Chen, F. Ye, P. Wu, L. Zhao, J. Wu, Y. Tu, Y. Zhang, X. Yang, W. Zhang, R. H. Friend, Q. Gong, H. J. Snaith, R. Zhu, *Science* **2018**, *360*, 1442.

[21] Z. Liu, L. Krückemeier, B. Krogmeier, B. Klingebiel, J. A. Márquez, S. Levcenko, S. Öz, S. Mathur, U. Rau, T. Unold, T. Kirchartz, *ACS. Energy Lett.* **2019**, *4*, 110.

[22] a) Y. Yang, M. Yang, David T. Moore, Y. Yan, Elisa M. Miller, K. Zhu, Matthew C. Beard, *Nat. Energy* **2017**, *2*, 16207; b) M. Stolterfoht, P. Caprioglio, C. M. Wolff, J. A. Marquez, J. Nordmann, S. S. Zhang, D. Rothhardt, U. Hormann, Y. Amir, A. Redinger, L. Kegelmann, F. S. Zu, S. Albrecht, N. Koch, T. Kirchartz, M. Saliba, T. Unold, D. Neher, *Energy Environ. Sci.* **2019**, *12*, 2778; c) C. M. Wolff, P. Caprioglio, M. Stolterfoht, D. Neher, *Adv. Mater.* **2019**, *31*, 1902762.

[23] J. T. Wang, G. Y. Jin, Q. Z. Zhen, C. Y. He, Y. Duan, *Adv. Mater. Interfaces* **2021**, *8*, 2002078.

[24] C. Bi, X. P. Zheng, B. Chen, H. T. Wei, J. S. Huang, *ACS Energy Lett.* **2017**, *2*, 1400.

[25] B. Roose, A. Ummadisingu, J. P. Correa-Baena, M. Saliba, A. Hagfeldt, M. Graetzel, U. Steiner, A. Abate, *Nano Energy* **2017**, *39*, 24.

[26] T. T. Ngo, E. M. Barea, R. Tena-Zaera, I. Mora-Sero, *ACS Appl. Energy Mater.* **2018**, *1*, 4057.

[27] J. P. Bastos, G. Uytterhoeven, W. Qiu, U. W. Paetzold, D. Cheyns, S. Surana, J. Rivas, M. Jaysankar, W. Song, T. Aernouts,

[28] a) F. Matsumoto, S. M. Vorpahl, J. Q. Banks, E. Sengupta, D. S. Ginger, *J. Phys. Chem. C.* **2015**, *119*, 20810; b) Z. Safari, M. B. Zarandi, M. R. Nateghi, *Chem. Pap.* **2019**, *73*, 2667; c) T. Mahmoudi, Y. Wang, Y.-B. Hahn, *ACS Energy Lett.* **2019**, *4*, 235.

[29] a) C.-W. Chen, H.-W. Kang, S.-Y. Hsiao, P.-F. Yang, K.-M. Chiang, H.-W. Lin, *Adv. Mater.* **2014**, *26*, 6647; b) Y. H. Lee, J. Luo, M.-K. Son, P. Gao, K. T. Cho, J. Seo, S. M. Zakeeruddin, M. Grätzel, M. K. Nazeeruddin, *Adv. Mater.* **2016**, *28*, 3966; c) D. H. Cao, C. C. Stoumpos, C. D. Malliakas, M. J. Katz, O. K. Farha, J. T. Hupp, M. G. Kanatzidis, *APL Mater.* **2014**, *2*, 091101.

[30] S. Moghadamzadeh, I. M. Hossain, M. Jakoby, B. A. Nejand, D. Rueda-Delgado, J. A. Schwenzer, S. Gharibzadeh, T. Abzieher, M. R. Khan, A. A. Haghighirad, I. A. Howard, B. S. Richards, U. Lemmer, U. W. Paetzold, *J. Mater. Chem. A* **2020**, *8*, 670.

[31] Y. Cho, H. D. Kim, J. H. Zheng, J. M. Bing, Y. Li, M. Zhang, M. A. Green, A. Wakamiya, S. J. Huang, S. Ohkita, A. W. Y. Ho-Baillie, *ACS Energy Lett.* **2021**, *6*, 925.

[32] M. Liu, M. Johnston, H. Snaith, *Nature* **2013**, *501*, 395.

[33] O. Malinkiewicz, A. Yella, Y. H. Lee, G. M. Espallargas, M. Graetzel, M. K. Nazeeruddin, H. J. Bolink, *Nat. Photonics* **2014**, *8*, 128.

[34] C. Momblona, L. Gil-Escrig, E. Bandiello, E. M. Hutter, M. Sessolo, K. Lederer, J. Blochwitz-Nimoth, H. J. Bolink, *Energy Environ. Sci.* **2016**, *9*, 3456.

[35] D. Kiermasch, L. Gil-Escrig, A. Baumann, H. J. Bolink, V. Dyakonov, K. Tvingstedt, *J. Mater. Chem. A* **2019**, *7*, 14712.

[36] B-S. Kim, L. Gil-Escrig, M. Sessolo, H. J. Bolink, *J. Phys. Chem. Lett.* **2020**, *11*, 6852.

[37] a) G. Divitini, S. Cacovich, F. Matteocci, L. Cinà, A. Di Carlo, C. Ducati, *Nat. Energy* **2016**, *1*, 15012; b) A. F. Akbulatov, S. Y. Luchkin, L. A. Frolova, N. N. Dremova, K. L. Gerasimov, I. S. Zhidkov, D. V. Anokhin, E. Z. Kurmaev, K. J. Stevenson, P. A. Troshin, *J. Phys. Chem. Lett.* **2017**, *8*, 1211.

[38] W. Tress, M. Yavari, K. Domanski, P. Yadav, B. Niesen, J. P. Correa Baena, A. Hagfeldt, M. Graetzel, *Energy Environ. Sci.* **2018**, *11*, 151.

[39] Q. Jiang, Y. Zhao, X. Zhang, X. Yang, Y. Chen, Z. Chu, Q. Ye, X. Li, Z. Yin, J. You, *Nat. Photonics* **2019**, *13*, 460.

[40] K. Tvingstedt, C. Deibel, *Adv. Energy Mater.* **2016**, *6*, 1502230.

[41] J. Benduhn, K. Tvingstedt, F. Piersimoni, S. Ullbrich, Y. L. Fan, M. Tropiano, K. A. McGarry, O. Zeika, M. K. Riede, C. J. Douglas, S. Barlow, S. R. Marder, D. Neher, D. Spoltore, K. Vandewal, *Nat. Energy* **2017**, *2*, 17053.

[42] S. Ullbrich, A. Fischer, Z. Tang, J. Ávila, H. J. Bolink, S. Reineke, K. Vandewal, *Phys. Rev. Appl.* **2018**, *9*, 051003.

[43] D. Kiermasch, A. Baumann, M. Fischer, V. Dyakonov, K. Tvingstedt, *Energ Environ. Sci.* **2018**, *11*, 629.

[44] a) O. Almora, C. Aranda, E. Mas-Marzá, G. Garcia-Belmonte, *Appl. Phys. Lett.* **2016**, *109*, 173903; b) M. Fischer, K. Tvingstedt, A. Baumann, V. Dyakonov, *ACS Appl. Energy Mater.* **2018**, *1*, 5129.

[45] a) C. Deibel, A. Wagenpfahl, V. Dyakonov, *Phys. Rev. B* **2009**, *80*, 075203; b) F. Deledalle, P. Shakya Tuladhar, J. Nelson, J. R. Durrant, T. Kirchartz, *J. Phys. Chem. C* **2014**, *118*, 8837.

[46] T. Kirchartz, J. Nelson, *Phys. Rev. B* **2012**, *86*, 165201.

[47] W. M. M. Lin, D. Bozyigit, O. Yarema, V. Wood, *J. Phys. Chem. C* **2016**, *120*, 12900.

[48] T. Du, J. Kim, J. Ngiam, S. Xu, P. R. Barnes, J. R. Durrant, M. A. McLachlan, *Adv. Funct. Mater.* **2018**, *28*, 1801808.

[49] L. M. Pazos-Outón, T. P. Xiao, E. Yablonovitch, *J. Phys. Chem. Lett.* **2018**, *9*, 1703.

[50] M. Fischer, AnnA.jl (Version 0.3.0) [Computer software], **2021**. https://doi.org/10.5281/zenodo.4733024.

[51] T. J. Jacobsson, L. J. Schwan, M. Ottosson, A. Hagfeldt, T. Edvinsson, *Inorg. Chem.* **2015**, *54*, 10678.

[52] a) E. Smecca, Y. Numata, I. Deretzis, G. Pellegrino, S. Boninelli, T. Miyasaka, A. La Magna, A. Alberti, *Phys. Chem. Chem. Phys.* **2016**, *18*, 13413; b) R. L. Milot, G. E. Eperon, H. J. Snaith, M. B. Johnston, L. M. Herz, *Adv. Funct. Mater.* **2015**, *25*, 6218.

[53] L. T. Schelhas, J. A. Christians, J. J. Berry, M. F. Toney, C. J. Tassone, J. M. Luther, K. H. Stone, *ACS Energy Lett.* **2016**, *1*, 1007.

[54] H. M. N. Ferdous, I. Nazifah, L. Zhen, R. Guofeng, Z. Kai, F. Zhaoyang, *ChemSusChem* **2016**, *9*, 2692.

[55] H. Tsai, R. Asadpour, J.-C. Blancon, C. C. Stoumpos, O. Durand, J. W. Strzalka, B. Chen, R. Verduzco, P. M. Ajayan, S. Tretiak, J. Even, M. A. Alam, M. G. Kanatzidis, W. Nie, A. D. Mohite, *Science* **2018**, *360*, 67.

[56] a) C. Zhu, X. Niu, Y. Fu, N. Li, C. Hu, Y. Chen, X. He, G. Na, P. Liu, H. Zai, Y. Ge, Y. Lu, X. Ke, Y. Bai, S. Yang, P. Chen, Y. Li, M. Sui, L. Zhang, H. Zhou, Q. Chen, *Nature Comm.* **2019**, *10*, 815;

b) T. W. Jones, A. Osherov, M. Alsari, M. Sponseller, B. C. Duck, Y.-K. Jung, C. Settens, F. Niroui, R. Brenes, C. V. Stan, Y. Li, M. Abdi-Jalebi, N. Tamura, J. E. Macdonald, M. Burghammer, R. H. Friend, V. Bulović, A. Walsh, G. J. Wilson, S. Lilliu, S. D. Stranks, *Energy Environ. Sci.* **2019**, *12*, 596.

[57] K. Nishimura, D. Hirotani, M. A. Kamarudin, Q. Shen, T. Toyoda, S. Iikubo, T. Minemoto, K. Yoshino, S. Hayase, *ACS Appl. Mater. Interfaces* **2019**, *11*, 31105.

[58] K. B. Lohmann, J. B. Patel, M. U. Rothmann, C. Q. Xia, R. D. J. Oliver, L. M. Herz, H. J. Snaith, M. B. Johnston, *ACS Energy Lett.* **2020**, *5*, 710.

[59] a) C. Yang, J. Wang, X. Bao, J. Gao, Z. Liu, R. Yang, *Electrochim. Acta* **2018**, *281*, 9; b) H. Zhang, X. Ren, X. Chen, J. Mao, J. Cheng, Y. Zhao, Y. Liu, J. Milic, W.-J. Yin, M. Grätzel, W. C. H. Choy, *Energy Environ. Sci.* **2018**, *11*, 2253.

[60] Y. Jiang, E. J. Juarez-Perez, Q. Ge, S. Wang, M. R. Leyden, L. K. Ono, S. R. Raga, J. Hu, Y. Qi, *Mater. Horiz.* **2016**, *3*, 548.